Research article

Xiaofei Zhao, Chundong Liu, Jing Yu, Zhen Li, Lu Liu, Chonghui Li, Shicai Xu, Weifeng Li, Baoyuan Man* and Chao Zhang*

Hydrophobic multiscale cavities for high-performance and self-cleaning surface-enhanced Raman spectroscopy (SERS) sensing

https://doi.org/10.1515/nanoph-2020-0454
Received August 6, 2020; accepted October 6, 2020; published online October 26, 2020

Abstract: Cavity array, with excellent optical capture capability, has received increasing attention for the surface-enhanced Raman spectroscopy (SERS)-active substrates. Here, we proposed molybdenum disulfide (MoS_2) nanocavities growing on pyramid Si (PSi) composed of in situ reduced Au nanoparticles (AuNPs), which can form the multiscale cavities (MSCs), and is facile for the couple of the plasmon. We demonstrated that the PSi/MoS_2/Au MSCs can serve as highly sensitive, uniform, and stable SERS substrates for rhodamine 6G (R6G), crystal violet, and adenosine triphosphate detection, benefiting from the synergistic effect of the enhanced light trapping and the effective plasmonic couple. The couple of the plasmon in the MSCs is evidently proved by finite-difference time domain simulation, showing the strong electromagnetic field is located around the cavity wall. Moreover, the excellent hydrophobicity of the PSi/MoS_2/AuNPs substrate endows it with the ability for the directional monitoring of organic pollutant in a mixture of oil and water. Finally, we demonstrated the MSCs with outstanding photocatalytic performance could achieve the renewable utilization by self-cleaning, which was attributed to the fast electron transfer and effective light absorption. The proposed PSi/MoS_2/AuNPs MSC represents a robust mean using the plasmonic metal/semiconductor heterostructure for high-performance SERS sensors and photodegradation.

Keywords: hydrophobic; multiscale cavities; self-cleaning; SERS sensing.

***Corresponding authors: Baoyuan Man**, Collaborative Innovation Center of Light Manipulations and Applications in Universities of Shandong School of Physics and Electronics, School of Physics and Electronics, Shandong Normal University, Jinan 250014, P.R. China, E-mail: byman@sdnu.edu.cn; and **Chao Zhang**, Collaborative Innovation Center of Light Manipulations and Applications in Universities of Shandong School of Physics and Electronics, School of Physics and Electronics, Shandong Normal University, Jinan 250014, P.R. China; and Institute of Materials and Clean Energy, Shandong Normal University, Jinan 250014, P.R. China, E-mail: czsdnu@126.com. https://orcid.org/0000-0002-3295-8980
Xiaofei Zhao, Chundong Liu and Lu Liu, Collaborative Innovation Center of Light Manipulations and Applications in Universities of Shandong School of Physics and Electronics, School of Physics and Electronics, Shandong Normal University, Jinan 250014, P.R. China
Jing Yu and Zhen Li, Collaborative Innovation Center of Light Manipulations and Applications in Universities of Shandong School of Physics and Electronics, School of Physics and Electronics, Shandong Normal University, Jinan 250014, P.R. China; and Institute of Materials and Clean Energy, Shandong Normal University, Jinan 250014, P.R. China
Chonghui Li, Collaborative Innovation Center of Light Manipulations and Applications in Universities of Shandong School of Physics and Electronics, School of Physics and Electronics, Shandong Normal University, Jinan 250014, P.R. China; and Institute for Integrative Nanosciences, IFW Dresden, Dresden, 01069, Germany
Shicai Xu, College of Physics and Electronic Information, Dezhou University, Dezhou 253023, P.R. China
Weifeng Li, School of Physics and State Key Laboratory of Crystal Materials, Shandong University, Jinan, Shandong, 250100, P.R. China

1 Introduction

Raman spectroscopy can give molecule-specific information about the chemical compound as nondestructive analysis tool. However, it is difficult to detect molecules at low concentration because of poor Raman cross-section area [1, 2]. To increase the sensitivity of Raman spectroscopy, various enhancement techniques such as resonance Raman spectroscopy [3], tip-enhanced Raman spectroscopy [4], and surface-enhanced Raman spectroscopy (SERS) [5–7] have been researched in the last few decades. Among them, SERS has been intensively considered as a powerful analysis technique for molecule detection at super-low concentration, even down to single molecule level, because the rational design of SERS substrates can be made to form abundant hot spots [8–10]. It is generally

accepted that the SERS effect for amplifying Raman signal arises from two mechanisms: localized electromagnetic field (electromagnetic mechanism with an enhancement factor [EF] of ~10^6–10^8) and charge-transfer complexes (chemical mechanism with an EF of ~10^2–10^4) [11, 12].

To greatly enhance the SERS performance, cavity structures have attracted increasing attention in the last few years, which can trap the laser, increase the light path, and further promote the interactions between photons and absorbed molecules [13]. Tian et al. prepared the bottom bowl-shaped silver cavity thin film layer by electrodeposition using polystyrene spheres as a template for SERS detection [14]. Hyungsoon et al. form self-assembled plasmonic nanoring cavity arrays alongside the curvature of highly packed metallic nanosphere gratings for SERS detection of the biological analyte and adenine [15]. Zuo et al. fabricated the conical silver nanocavity by depositing Ag with different thickness on porous alumina templates with V-shaped nanopores [16]. However, these methods commonly require complex fabrication processes with all kinds of templates, which has greatly limited the practical application for high-performance and reliable SERS substrates. As we all know, semiconductor-based SERS substrates have been one of the most popular materials because of their novel optoelectronic and nanoelectronic properties [17]. Especially, molybdenum disulfide (MoS_2) possesses catalytic activity at edge sites with the inert characteristic, which is considered as a catalyst and a promising supporting material [18]. Various techniques have been adopted to fabricate MoS_2 by lithium intercalation [19], mechanical exfoliation [20], or thermal decomposition [21]. Most of these programs are complicated and dangerous and hard to control the size, shape, and dimension.

In the light of the aforementioned problems, we directly grow 3D MoS_2 nanocavity over pyramid Si microstructure by hydrothermal synthesis to form the multiscale cavities (MSCs) and increase the number of exposed active edge sites for compositing with Au nanoparticles (AuNPs) to further enhance the SERS sensor signal (named as pyramid Si [PSi]/MoS_2/Au MSCs). The hydrothermal method could control over the morphology effectively and exempt from the high temperature and toxic gases [22]. Here, the green and convenient method has been developed to fabricate the MoS_2 cavities with appropriate surface roughness and active sites, which can promote in situ growth of AuNPs on MoS_2 nanosheets' surface. The proposed MSC structure possesses excellent optical capture capability and can further facilitate the interactions between photons and absorbed molecules. The SERS capabilities can be optimized by tailoring the particle density and size in the MoS_2 cavity configurations introducing extra "hot spots" to generate strong electromagnetic field enhancement. It is found that the as-fabricated substrate is highly efficient to detect rhodamine 6G (R6G), crystal violet (CV), and adenosine triphosphate (ATP) molecules at low concentration because of the light trapping of MSC structure and formation of denser "hot spots". In addition, the as-prepared MSCs possess excellent hydrophobicity after decoration with AuNPs, which can realize directional monitoring in oil-water-mixed solution. The excellent photocatalysis of the prepared substrate can effectively degrade organic pollutants, which makes it possible to achieve the renewable utilization by self-cleaning feature attributed to effective absorption of visible light, abundant exposed catalytic active sites, and fast electron transfer. This hybrid sensor that uses the combination of MoS_2 and AuNPs will expand the application of the semiconductor and gain a better understanding of their basic properties.

2 Experimental section

2.1 Preparation of PSi/MoS_2 MSCs

A PSi substrate with a size of 1×1 cm^2 was fabricated by the wet texturing technology with the aid of the anisotropic etching property, which was described in our early work [23]. The PSi samples with the same size were cleaned by acetone, alcohol, and deionized water (DI water) for 20 min in sequence in an ultrasonic cleaner. The 3D MoS_2 nanosheets were synthetized on the PSi substrate by a facile one-step hydrothermal method. Briefly, $Na_2MoO_4{\cdot}2H_2O$ (1.69 g) and CH_4N_2S (2.28 g) were dissolved in a mixed solution of DI water (15 mL) and ethanol (15 mL) under vigorous stirring, and then the mixed solution was transferred into a 50-mL Teflon-lined stainless steel autoclave. The PSi substrate was gently placed in the autoclave, which was heated at 180 °C for 7 h after sealed with a lid and then cooled to room temperature naturally. The resultant PSi/MoS_2 MSCs were washed with DI water continuously and then dried under vacuum at room temperature.

2.2 Decoration of AuNPs in the PSi/MoS_2 MSCs

The AuNPs were decorated on the MoS_2 nanosheets to form PSi/MoS_2/Au hybrid MSCs by in situ reduction reaction of $HAuCl_4$. In this process, the prepared PSi/MoS_2 substrates were immersed in 1-mM $HAuCl_4$ with different reaction times of 1, 2, 3, 4, and 5 min to generate AuNPs and then transferred into DI water to remove residual $HAuCl_4$. At last, the PSi/MoS_2/AuNPs MSC substrates were dried at room temperature.

2.3 Apparatus and characterization

The structure and morphologies of the prepared samples were studied by the scanning electron microscope (SEM) (ZEISS Sigma500 at 5.0 kV) with energy-dispersive spectrometer (EDS) (at 20 kV operated at 200 kV). The more detailed morphology and composition were characterized by transmission electron microscope (TEM, JEM-2100F) and a high-resolution TEM (HRTEM) equipped with selected area electron diffraction (SAED). X-ray diffraction (XRD) (SmartLab9) pattern was recorded to identify the crystal phase with Cu-Kα radiation. X-ray photoelectron spectroscopy (XPS) (Thermo Fisher Scientific 250Xi) was carried out to analyze surface chemicals, composition, and the valence state of prepared substrate.

2.4 SERS spectrum measurement

R6G and CV molecules were successively diluted with alcohol solution from the concentration of 10^{-3} to 10^{-11} M by factors of 10, and 4 μL of the molecule solution was dropped on the surface of the substrate and dried up naturally before SERS detection. The average intensities of the Raman signal at random six positions on the substrate were used to reduce measurement errors. SERS spectra were performed on a Raman spectrometer (Horiba HR Evolution 800) at a laser wavelength of 532 nm. To reduce the photocatalytic and photochemical degradation caused by laser illumination, the laser power was set as 0.48 mW with an integration time of 4 s and diffraction grid of 600 g/nm. A 50× objective was used to focus the laser beam on the substrate.

2.5 Recyclable SERS detection

First, we dropped 10^{-7}M R6G on the PSi/MoS_2/AuNPs MSC samples and collected the SERS signal. After that, we immersed MSC samples in the DI water and irradiated it with a 300-W xenon lamp with a cut-off filter (λ > 420 nm) as a visible light source. The distance between the sample and the light was 20 cm. The sample was taken out from the DI water every 15 min and rinsed with the clean DI water several times to remove residual molecules and dried at room temperature. The degradation of R6G was monitored by measuring its SERS spectra until no SERS signal was detected. The substrate was reused for detection and photocatalysis of R6G molecules three times.

2.6 FDTD simulations

The reflection spectra and the electromagnetic field distributions were simulated with finite-difference time domain (FDTD) simulation. In theoretical simulations, the absorption boundary condition is the perfect matching layer. A linearly polarized monochromatic plane wave with 532-nm wavelength was irradiated onto the sample with the polarization along the *x*-direction. The geometrical parameters of the structures were obtained from the SEM measurements with an average 12-nm wall thickness, 150-nm length, and 100-nm pore calibre of MoS_2 nanocavity and an average diameter of 8 nm and interparticle gap of 3 nm for AuNPs. The average height and average space for PSi are 3 and 4 μm, respectively. A mesh size of 0.8 nm for all axes was used. The refractive index data of MoS_2 were obtained from Beal and Huges [24]. The dielectric data of Au and Si were from the studies by Babar and Weaver and Schinke et al. respectively [25, 26].

3 Results and discussion

The morphology of the as-grown MoS_2 nanosheets on PSi was characterized with SEM, where we can observe the MSCs clearly (PSi microcavity and MoS_2 nanocavity), as shown in Figure 1A. After hydrothermal treatment for 7 h, the vertical MoS_2 exhibits closely aligned flake-like structure with an average 12-nm wall thickness and 100-nm pore calibre, which is tightly attached on the PSi surface and forms the nanocavities. After the MoS_2 nanosheets react with $HAuCl_4$, denser AuNPs were decorated on the surface of MoS_2 nanosheets with an average diameter of 8 nm and an interparticle gap of 3 nm as presented in Figure 1B. The vertically growing MoS_2 nanosheets decorated with AuNPs on the PSi presents a MSC, which can effectively trap light and improve the utilization of light. To further validate the combination of the metallic particle and semiconductor materials, TEM is performed as shown in Figure 1C, where the AuNPs and MoS_2 can be clearly observed, indicating that the MoS_2 nanosheets can act as an efficient substrate for the nucleation and growth of AuNPs. Moreover, the HRTEM in Figure 1D was measured to further analyze detail structures, where the size of AuNPs is consistent well with that in SEM. The two distinct interlayer spacing with values of 0.62 and 0.23 nm is in agreement with the (002) plane of MoS_2 nanosheets and the main (111) plane of AuNPs, respectively. The SAED pattern of the hybrid is shown in Figure 1E, in which the diffraction rings of MoS_2 (002) and Au (111) are well indexed to that observed in HRTEM, and the 004 and 106 planes of MoS_2 can also been identified

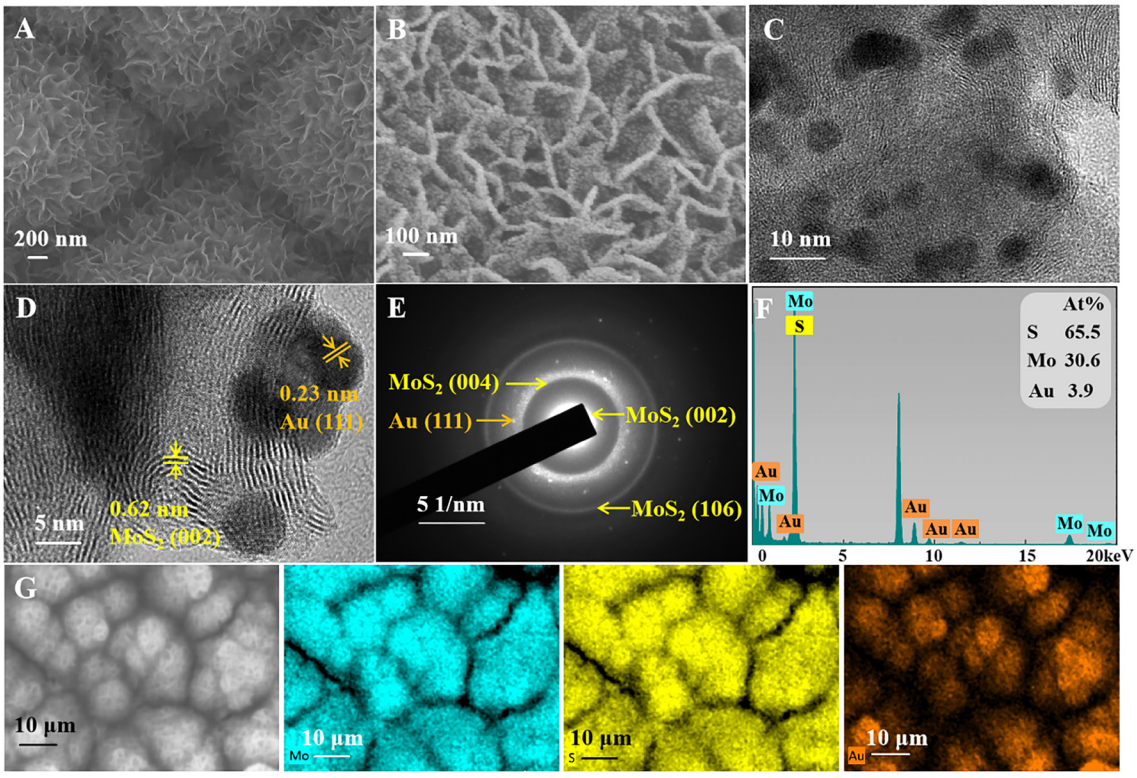

Figure 1: Structural characterization of molybdenum disulfide (MoS_2)-based substrates.
Scanning electron microscope (SEM) morphology characterization of (A) pyramid Si (PSi)/MoS_2 and (B) PSi/MoS_2/Au multiscale cavity (MSC) substrate. (C) Transmission electron microscope (TEM) image of Au nanoparticles (AuNPs) decorated on the MoS_2 nanosheets. (D) High-resolution transmission electron microscope (HRTEM) image of AuNPs decorated on the MoS_2 nanosheets. (E) The selected area electron diffraction (SAED) pattern of MoS_2/Au. (F) The corresponding energy-dispersive spectrometer (EDS) spectrum. (G) EDS elemental maps from Mo, S, and Au on the PSi/MoS_2/Au MSC sample.

from Figure 1E with lattice spacing of 0.31 and 0.16 nm. Furthermore, the corresponding EDS spectra of TEM in Figure 1F prove the distribution and coexistence of S, Mo, and Au elements, and the atomic contents are 65.5, 30.6, and 3.9% of Mo, S, and Au, respectively. The local composition of the sample is also measured with EDS elemental mappings of SEM shown in Figure 1G, which clearly reveals the presence of Mo (blue), S (yellow), and Au (orange) in the substrate. All the characteristics strongly demonstrate the heterostructure of MoS_2 and Au is successfully synthesized.

XPS spectra were carried out to analyze the elemental composition and chemical states of the PSi/MoS_2/Au MSC substrates quantitatively and qualitatively. Figure 2A depicts the XPS survey spectrum of the substrate, where besides the C 1s (285.0 eV) and O 1s (532.5 eV), the Mo, S, and Au elements are all presented among the spectra. Figure 2B–D presents the high-resolution spectra of the Mo 3d, S 2p, and Au 4f regions of PSi/MoS_2/Au MSC substrates, respectively. As shown in Figure 2B, the high-resolution XPS scan of Mo 3d identified the two characteristic peaks at 229.14 and 232.36 eV arising from the Mo $3d_{5/2}$ and Mo $3d_{3/2}$ orbital, which suggests that the IV oxidation state of Mo^{4+} plays a dominant role in the MoS_2 matrix [27]. Besides, the S 2s peak corresponds to 226.34 eV, and Mo^{6+} peak at 236.08 eV (caused by the oxidation of the MoS_2 surface) was also obvious [28]. Meanwhile, in the high-resolution S 2p spectrum of Figure 2C, there are two separated peaks at 163.19 and 162.09 eV, respectively, assigned to the S $2p_{1/2}$ and S $2p_{3/2}$ orbital of divalent sulfide ions (S^{2-}) derived from MoS_2 [21]. In Figure 2D, the two peaks of Au $4f_{5/2}$ and Au $4f_{7/2}$ at 88.27 and 84.57 eV supported the insertion of crystallized Au [29]. Furthermore, the XRD patterns of PSi/MoS_2 and PSi/MoS_2/Au MSC in Figure 2E are presented to better understand the structural information and element composition, in which both samples possess the almost same diffraction peaks (marked by blue pentagram) at 35.84° and 58.11°, corresponding to the 102 and 110 planes of MoS_2. There is a significant peak of PSi/MoS_2 XRD spectra at 29.20° corresponding to MoS_2 (004) planes, which is also obvious in SAED (Figure 1E). The three characteristic peaks of PSi/MoS_2/Au MSC (marked by orange shuriken) at 38.26°, 44.40°, and 64.75° are clearly noticed, corresponding to the

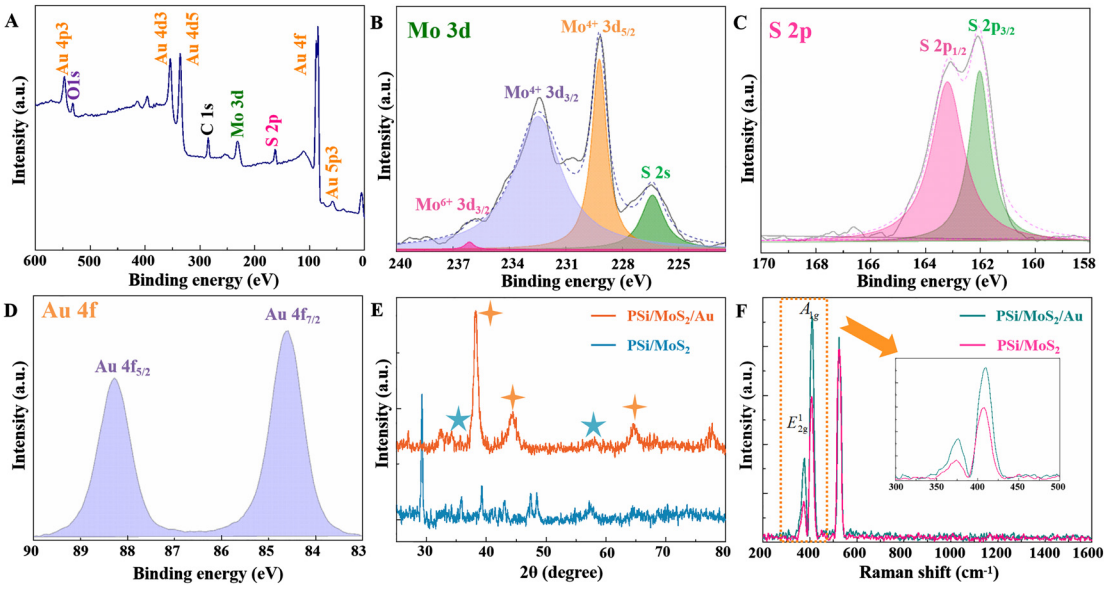

Figure 2: X-ray photoelectron spectroscopy (XPS), X-ray diffraction (XRD), and correspondingly surface-enhanced Raman spectroscopy (SERS) comparison.
XPS spectra in (A) survey, (B) Mo 3d, (C) S 2p, and (D) Au 4f regions of pyramid Si (PSi)/ molybdenum disulfide (MoS_2)/Au multiscale cavity (MSC) substrates. (E) XRD patterns of different samples: PSi/MoS_2, and PSi/MoS_2/Au. (F) SERS spectra of MoS_2 on PSi/MoS_2 MSC and PSi/MoS_2/Au MSC substrate.

111, 200, and 220 planes of Au, indicating the formation of AuNPs. A comparison of Raman spectra from 200 to 1600 cm^{-1} of the MoS_2 from PSi/MoS_2 and PSi/MoS_2/Au MSC substrate is displayed in Figure 2F. The pristine PSi/MoS_2 MSC exhibits two representative vibration peaks at around 378 and 406 cm^{-1}, assigned to the in-plane vibrations of Mo and S atoms (E^1_{2g}) and the out-of-plane lattice vibration of S atoms (A_{1g}), respectively [30], where no other background Raman signal is detected except for Si at 521 cm^{-1}. From the detailed inset of Figure 2F, it can be clearly observed the Raman modes of the pristine sample suffers a red shift by about 2 cm^{-1} after introduction of AuNPs on the MoS_2 nanosheets, indicating a strong interaction between the AuNPs and the MoS_2 nanosheets [31]. Furthermore, the intensity of the two characteristic peaks has enhanced after decoration with AuNPs, which can be ascribed to the strong electromagnetic field and denser "hot spots" arising from AuNPs. In brief, the aforementioned characterizations demonstrated the success of the MoS_2/Au hybrid structure, which could be used in the following SERS detection.

To explore the optimized SERS effect of PSi/MoS_2/Au MSC, MoS_2 nanosheets were reacted with $HAuCl_4$ at different times, as characterized in Figure 3. When the reaction time is 1 min, there are only patchy AuNPs loaded on the MoS_2 nanosheets (Figure 3B) compared with pristine PSi/MoS_2 (Figure 3A), and the size of AuNPs is not uniform, which is in the early stages of nucleation. With the reaction time up to 2 min, the AuNPs become bigger than that of 1 min but still sparse around MoS_2 nanosheets as shown in Figure 3C. Further increasing the time to 3 min, the vertical MoS_2 nanosheets were evenly covered by dense AuNPs (Figure 3D), and the space between AuNPs was quite narrow, forming MoS_2-AuNPs composite cavities. With the further increase of the reaction time to 4 min, the MoS_2 nanosheets are all hid under the Au film but still retained sheet structure as shown in Figure 3E. When the reaction time was up to 5 min, the structure of MoS_2 cavities is not obvious, which is filled with the thick Au (Figure 3F). Based on the aforementioned experiment, it is clear that the MoS_2 cavities were gradually covered by more and more Au with the increase of the reaction time, which is a key factor that affects the morphology and performance of the composite substrate.

Figure 4A shows the change of the Raman signal intensity for R6G alcoholic solution (10^{-5}M) detected on the PSi/MoS_2/Au MSC with increasing the reaction time from 1 to 5 min. The reason to choose the R6G alcoholic solution is that the excellent hydrophobicity of the proposed MSC structure makes the water solution hardly load in the cavity, which will be further discussed in the following section. It is apparent the SERS activity enhances with an increasing reaction time from 1 to 3 min because of the formation of more and more AuNPs around MoS_2 cavities and decreases with further increasing the time from 3 to 5 min probably because of excessive aggregation of AuNPs, which will

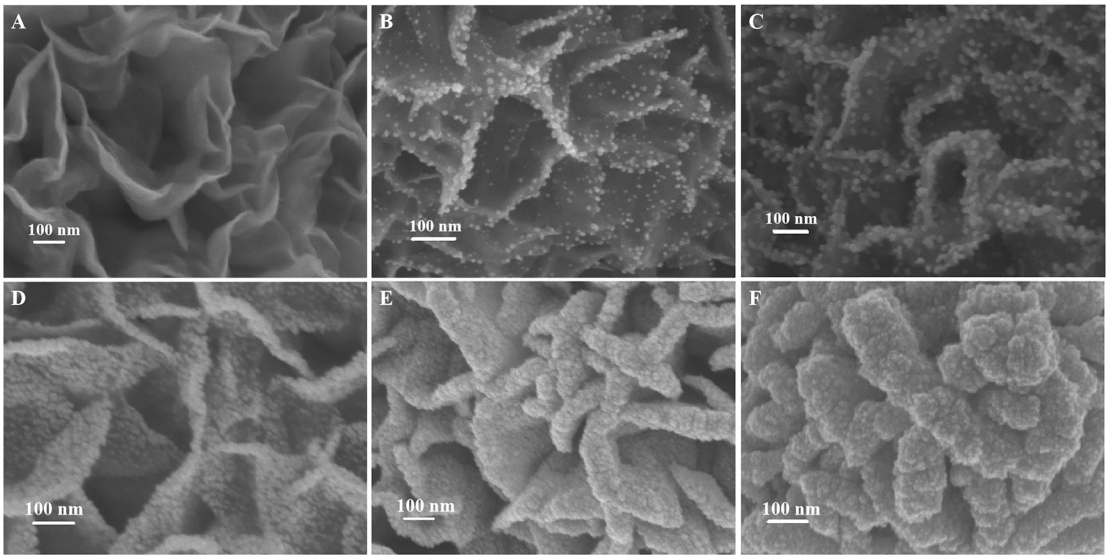

Figure 3: Scanning electron microscope (SEM) images of molybdenum disulfide (MoS_2)-based substrate.
SEM images of (A) pyramid Si (PSi)/molybdenum disulfide (MoS_2) multiscale cavity (MSC) with magnification; (B–F) PSi/MoS_2/Au MSC with different reaction times of $HAuCl_4$ at 1, 2, 3, 4, and 5 min.

weaken the plasmonic couple. Therefore, it can conclude the optimal SERS performance is obtained at a reaction time of 3 min, which is maintained to further research throughout the following experiments. As a contrast, Raman spectra of R6G absorbed on pristine PSi/MoS_2 MSC in Figure 4B were detected with the limit of detection (LOD) of 10^{-6}M, which can be ascribed to the weak charge-transfer mechanism [32]. After loading AuNPs inside the MoS_2 cavities at a reaction time of 3 min, the baseline-corrected Raman peak of R6G with different concentrations from 10^{-5} to 10^{-11}M is drawn, Figure 4C, in which the main characteristic peaks at 613, 774, and 1650 cm^{-1} are assigned to the C–C–C deformation in-plane vibration, out-of-plane bending, and aromatic C–C stretching, respectively [33, 34]. Although the Raman intensity of R6G is reduced with the decrease in R6G concentration, the characteristic peaks can still be observed at concentrations as low as 10^{-11}M, and the LOD is five orders of magnitude lower than that of pristine PSi/MoS_2 MSC. Figure 4D presents the intensity with error bar (from same sample but different positions) at 613, 774, and 1650 cm^{-1} as a function of the R6G concentrations under the log scale, which, respectively, fits the linearity well with correlation coefficient (R^2) values of 0.997, 0.996, and 0.974, thus having a great potential for sensitive and quantitative detection of the dye. To evaluate the role of MoS_2 nanocavity, the SERS performance of PSi/Au substrate was compared with PSi/MoS_2/Au MSC. Here, we use the thermal evaporation method to deposit the same-size AuNPs on PSi with a diameter of 8 nm (Figure S1A), the SERS intensity of 10^{-5} M R6G on PSi/Au is much weaker than PSi/MoS_2/Au MSC (Figure S1B), suggesting MoS_2 nanocavities play an important role in SERS detection, which can form a focusing field for light trapping and further improve the SERS sensitivity. In addition, the SERS performance of PSi/MoS_2 and PSi/MoS_2/Au MSC is compared more intuitively in Figure S1B; it can be observed that the intensity of 10^{-5} M R6G on PSi/MoS_2/Au MSC has much enhanced than PSi/MoS_2 because of the localized surface plasmon resonance (LSPR) of AuNPs.

To quantize the SERS performances of the PSi/MoS_2/Au MSC, the EF was evaluated using the formula [35]:

$$\mathrm{EF} = \frac{I_{\mathrm{SERS}}/N_{\mathrm{SERS}}}{I_{\mathrm{RS}}/N_{\mathrm{RS}}}$$

where I_{SERS} and I_{RS} represent the intensity of SERS spectra and normal Raman and N_{SERS} and N_{RS} refer to the average number of molecules within the laser spot excited by SERS and normal Raman, respectively. Here, the value of $N_{\mathrm{RS}}/N_{\mathrm{SERS}}$ was estimated with the ratio of the respective molecule concentrations [36]. The minimum detection concentration is 10^{-11}M and the intensity of the SERS peak at 613 cm^{-1} is 64, whereas for normal Raman, the intensity of 10^{-3}M R6G on SiO_2 flake is 98. Consequently, the EF of the PSi/MoS_2/Au MSC is calculated as 6.5×10^7. Compared with other MoS_2/Au substrates in Table 1, PSi/MoS_2/Au MSC possesses a higher EF and sensitivity by virtue of the MSC structure. The excellent sensitivity of the prepared substrate can be attributed to ultranarrow nanogaps between AuNPs and a strong focusing field within the MSCs.

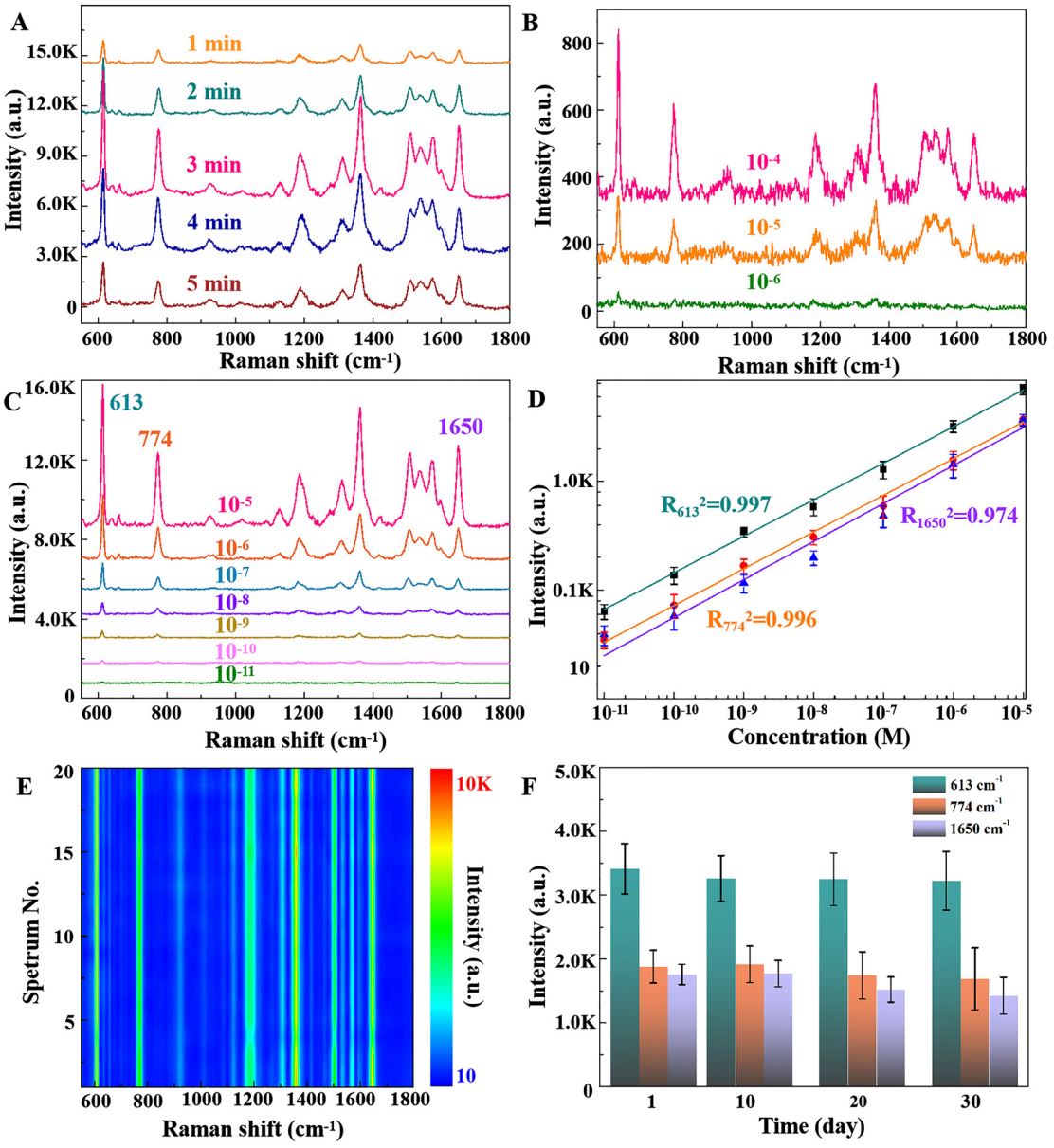

Figure 4: Surface-enhanced Raman spectroscopy (SERS) performance of R6G on different substrates.
(A) Raman spectra of R6G alcoholic solution (10^{-5} M) detected on the pyramid Si (PSi)/molybdenum disulfide (MoS_2)/Au multiscale cavity (MSC) with different reaction time. (B) Raman spectra of R6G alcoholic solution from 10^{-4} to 10^{-6}M on the PSi/MoS_2 MSC substrate. (C) Raman spectra of R6G (the concentration from 10^{-5} to 10^{-11}M) on the PSi/MoS_2/Au MSC SERS substrate. (D) Linear relationships: Raman intensities at 613, 774, and 1650 cm^{-1} as a function of the concentrations of R6G molecules. (E) The contour image of R6G (10^{-5}M) detected at 20 random positions on PSi/MoS_2/Au MSC SERS sample. (F) The stability: The intensity of three main characteristic peaks (10^{-6}M) detected on the PSi/MoS_2/Au MSC SERS substrate per 10 day.

The homogeneity is an important index for SERS substrate apart from sensitivity, which was proved by the contour in Figure 4E. This graph is made up of the intensity of 10^{-5}M R6G detected from 20 positions at the PSi/MoS_2/Au MSC, where the same colour presents the same intensity. To better illustrate the uniformity, the relative standard deviation of the intensity at 613, 774, and 1650 cm^{-1} was calculated with value of 4.15, 9.76, and 13.24%, respectively, shown in Figure S2A. Moreover, we have randomly selected a region of 20 × 20 μm^2 to measure the mapping at 613 cm^{-1} of 10^{-5}M R6G molecules dispensed on the PSi/MoS_2/Au MSC substrates, which shows a small fluctuation in Figure S2B. It can be concluded the SERS substrate possesses outstanding homogeneity, ascribing to the uniform distribution of AuNPs. Furthermore, we also verify the stability of the PSi/MoS_2/Au MSC for SERS

Table 1: The sensitivity of different MoS_2/Au SERS substrates.

Substrate	Analytes	EF	References
AuNPs@MoS_2-3 nanocomposite	R6G	8.2×10^5	[18]
1T-2H MoS_2/Au heterostructure	R6G	8.1×10^6	[31]
3D glass fiber-MoS_2@AuNP	CV	1.3×10^6	[37]
MoS_2 nanoflowers/AuNPs	R6G	1.69×10^7	[38]
PSi/MoS_2/Au MSC	R6G	6.5×10^7	This work

AuNPs, Au nanoparticles; CV, crystal violet; MoS_2, molybdenum disulfide; MSC, multiscale cavity; PSi, pyramid Si; SERS, surface-enhanced Raman spectroscopy.

detection in Figure 4F. The intensity of three main R6G characteristic peaks with error bar (from the same sample but a different position) at 613, 774, and 1650 cm^{-1} is presented with placement time per 10 days, which is almost no change by the virtue of the outstanding inertia of AuNPs. In general, the PSi/MoS_2/Au MSC has great promise in SERS application for low-concentration molecular detection.

To illustrate the practicability of the PSi/MoS_2/Au MSC, the CV alcoholic solution was detected on the SERS substrate with different concentrations from 10^{-5} to 10^{-10}M, and the corresponding SERS spectra are shown in Figure 5A. It can be observed that the Raman signal gradually diminishes when the CV concentration decreases from 10^{-5} to 10^{-10}M, and the main characteristic peaks can still be clearly identified even when the concentration reaches 10^{-10}M. As shown in Figure S3, a well-defined linear relationship can be obtained with a R^2 values of 0.997, 0.998, and 0.995 corresponding to 913, 1175, and 1620 cm^{-1}, respectively. In addition, the Raman spectra of ATP from 10^{-5} to 10^{-9}M were also measured in Figure 5B, which play important roles in energy storage and signaling of biological information. The characteristic peaks of ATP at 719, 1300, and 1330 cm^{-1} are clearly observed even down to 10^{-9}M. These results assure that the PSi/MoS_2/Au MSC hybrid substrate can be a potential SERS matrix in practical applications with excellent sensitivity because of the multiple reflection and scattering of electromagnetic waves.

The MSC structure can effectively trap incident light, improve the utilization of light, and couple with the plasmon across a wide spectral range, which is revealed by the reflectance spectrum in Figure 5C. The PSi substrate presents the highest reflectance relative compared with PSi/MoS_2 MSCs and PSi/MoS_2/Au MSCs. And, simulated PSi reflection spectrum (dashed line) by an FDTD method is calculated, where the two resonances, located at 234 and 338 nm indicated by the pink arrows, fairly agree with the measured result. The measured PSi/MoS_2 and PSi/MoS_2/Au MSCs all have the low reflectance in the whole wavelength region, implying more intense light utilization in the MSCs. Especially, there is a plasmon resonance of PSi/MoS_2/Au MSCs at about 500 nm (indicated by the blue arrows) corresponding to the Raman excitation wavelength of 532 nm because of the decoration of denser AuNPs.

To better understand the enhancement mechanism of this PSi/MoS_2/Au MSC SERS-active substrate, the local electric field distributions at *x-z* cross-section of the structures were analyzed by the FDTD simulations. The ability of micron-size pyramidal cavity for light trapping has been explored and demonstrated in our previous work [21, 23]. Consequently, here we only research the electric field distributions of the nanocavities with trumpet-like shape and rectangular shape, which represents the multiform nanostructure according to the SEM morphology. The local electric field distributions of the pristine MoS_2 cavity are illustrated in Figure 5D and F, where the electric field is concentrated within the cavities because of the aggregation of incident light. The MoS_2/Au cavities in Figure 5E and G present a similar focusing field as the pristine MoS_2 cavity, although with the relatively strong field strength. Interestingly, the higher near-field enhancements exists at tip in Figure 5E because the field is transformed into a propagating plasmon and transported from the apex along the taper in the reverse direction with excellent nanofocusing ability [39–41]. Furthermore, the maximum intensity of the focusing field is located around the AuNPs and between the adjacent gaps in cavity, which can attribute to the strong coupling between the cavity mode and the localized surface plasmons of the AuNPs. Therefore, abundant hot spots are generated on the sidewalls of cavity where the probe molecules are adsorbed, contributing to the excellent SERS activity of the PSi/MoS_2/Au MSC array.

Furthermore, except for the excellent light capture capability of MSCs, the MSC structure endows it with versatile hydrophobic performance, which was investigated on the PSi, PSi/MoS_2 MSC, flat-Si/MoS_2/Au, and PSi/MoS_2/Au MSC substrate. As shown in Figure 6A, the water contact angle on PSi is about 77°, which demonstrates its hydrophilic substrate due to the fairly smooth surface of the PSi (the morphology of the PSi is in the inset of Figure 6A). However, after the MoS_2 cavities covered on PSi, the water contact angle decreases to 38°, which was in the Wenzel state (Figure 6B). Even more striking, the angle reaches to 148° (in Cassie state) with excellent hydrophobicity after modified by denser AuNPs (Figure 6D). That is a significant difference between them, which can be verified from the morphology of the two substrates. The pristine MoS_2 cavities are composed of very thin nanosheets (shown in Figure 3A), where the structure is like soft villus unable to

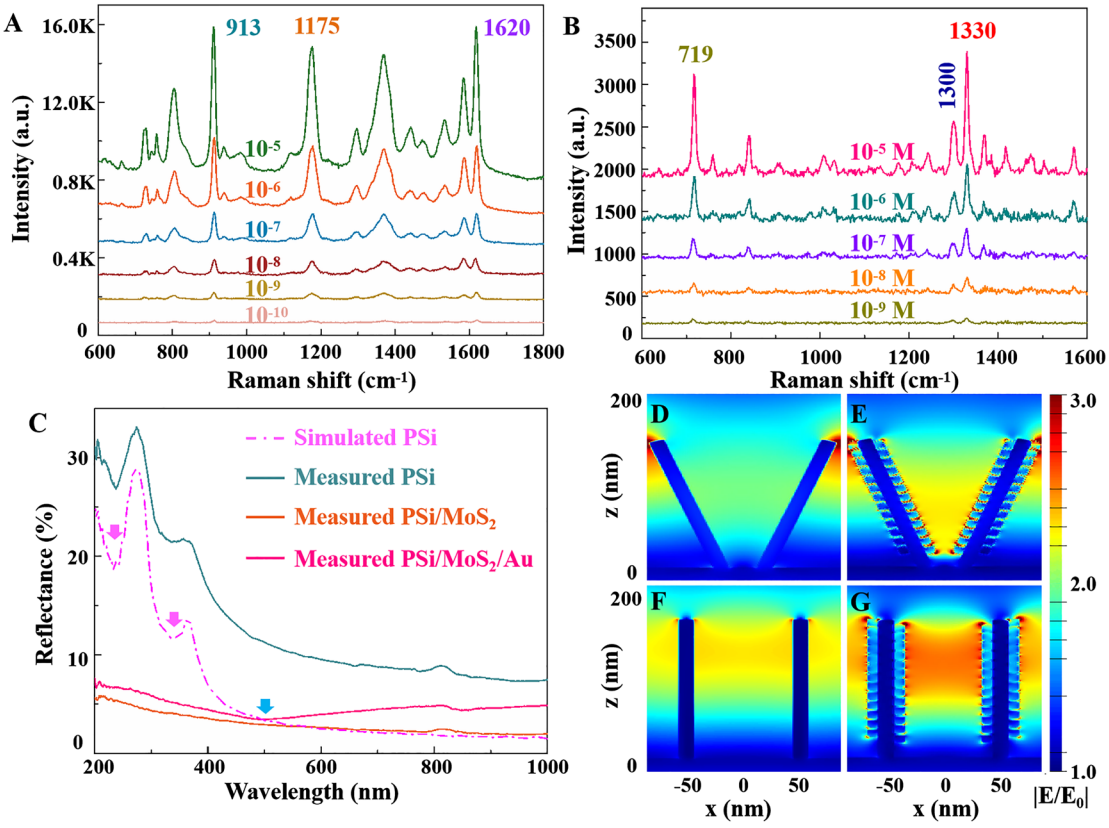

Figure 5: Surface-enhanced Raman spectroscopy (SERS) performance of crystal violet (CV) and electric field distribution. Raman spectra of (A) CV alcoholic solution (B) adenosine triphosphate on the pyramid Si (PSi)/ molybdenum disulfide (MoS_2)/Au multiscale cavity (MSC). (C) Reflectance spectrum of simulated PSi, measured PSi, PSi/MoS_2 MSC, and PSi/MoS_2/Au MSC. Simulated vertical electric field distribution of (D) banked MoS_2 cavity, (E) banked MoS_2/Au cavity, (F) vertical MoS_2 cavity, and (G) vertical MoS_2/Au cavity.

support the water droplet, promoting the extension of the water droplet instead. For PSi/MoS_2/Au MSCs, the vertical nanosheets become much stronger with the assistance of abundant AuNPs (shown in Figure 3D), which can make the water droplet keep on it. Furthermore, the hydrophobicity of the flat-Si/MoS_2/Au single-scale cavities was measured as a contrast shown in Figure 6C, where the water contact angle is about 140°, slightly smaller than that of PSi/MoS_2/Au MSC, which manifested the MSCs are the most pre-eminent hydrophobic sample. To further explore the characteristic in the SERS field, we mix the R6G aqueous solution and Sudan 1 toluene solution for detection. The PSi/MoS_2 MSC could detect R6G aqueous solution (10^{-5}M) and Sudan 1 toluene solution (10^{-3}M), which was dropped on the substrate, and their Raman spectra can be clearly observed in Figure 6E. To measure the hydrophobicity, the PSi/MoS_2 MSC was rapidly immersed in the mixture of the two molecules after vigorously shaking to make it contact fully with the oil/water solution because of the oil-water separation under its natural state. The characteristic peak of R6G and Sudan 1 can be detected from the PSi/MoS_2 MSC, which is labeled by the corresponding frame, proving the hydrophilic and oil-wet properties. As a contrast, the PSi/MoS_2/Au MSC was used for measuring the R6G aqueous solution (10^{-9}M), Sudan 1 toluene solution (10^{-5}M), and their mixture as shown in Figure 6F (R6G aqueous solution and Sudan 1 toluene solution are dropped on substrate, and the mixture is immersed by the sample). Unsurprisingly, the peaks of individual R6G and Sudan 1 dropped on it can all be detected on the hybrid sample, and there is only the Sudan 1 in the mixture that can be detected, which showed favourable hydrophobicity, which is the reason why we choose an alcoholic solution to dilute R6G and CV molecule for SERS detection. Above all, the PSi/MoS_2/Au MSC has a great potential for directional SERS detection in a complex mixture of oil and water.

Except for the hydrophobic properties, photocatalytic degradation of R6G was carried out to investigate performance of a recyclable SERS substrate. Figure 7A shows the SERS spectra of R6G (10^{-7}M) on the PSi/MoS_2/Au MSC irradiated by visible light with an interval of 15 min. The

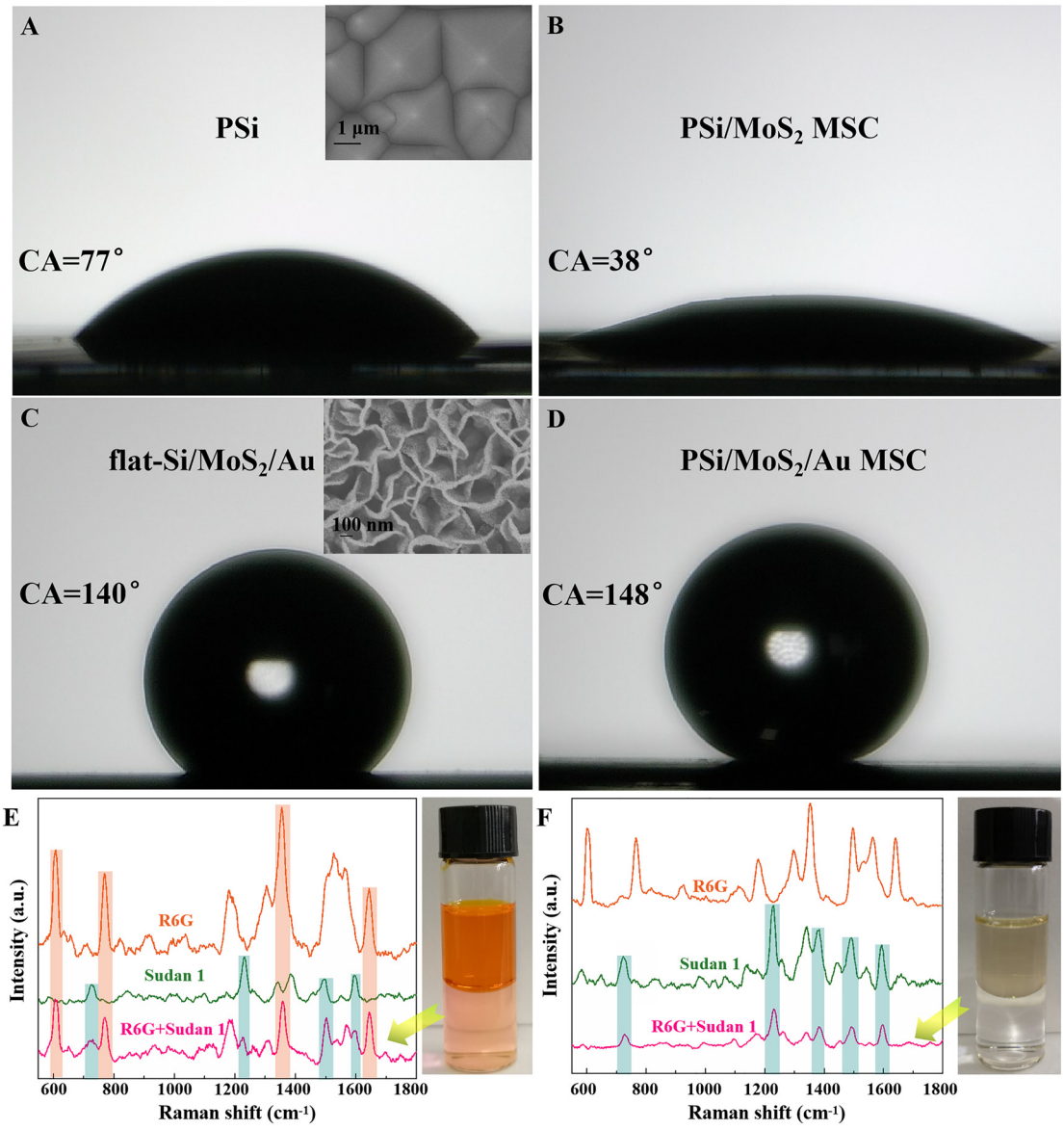

Figure 6: Hydrophobicity study of different samples.
The images about hydrophobicity of (A) pyramid Si (PSi) sample (the inset shows the corresponding scanning electron microscope [SEM] image of PSi), (B) PSi/molybdenum disulfide (MoS_2) multiscale cavity (MSC), (C) flat-Si/MoS_2/Au (the inset shows the corresponding SEM image), and (D) PSi/MoS_2/Au MSC. (E) The surface-enhanced Raman spectroscopy (SERS) spectra of R6G aqueous solution (10^{-5}M), Sudan 1 toluene solution (10^{-3}M) and their mixture detected from PSi/MoS_2 MSC. (F) The SERS spectra of R6G aqueous solution (10^{-9}M), Sudan 1 toluene solution (10^{-5}M), and their mixture detected from PSi/MoS_2/Au MSC. The two photos at right are the mixture of R6G aqueous solution and Sudan 1 toluene solution.

intensity of R6G peaks gradually decreased with the increase of irradiation times and completely disappeared after 105 min of photodegradation. The intensity of the Raman peak at 613 cm^{-1} is shown in Figure 7B, which was used as an indicator of the self-cleaning ability with different irradiation times from 0 to 105 min. And, the same peak was also counted under dark condition, which almost has no change over time, proving the attenuation of intensity is caused by photodegradation. Moreover, Figure 7C shows the results for R6G collected at the initial SERS detection and after self-cleaning treatment. After visible light exposure at 120 min, no characteristic peaks of R6G were observed, which can be ascribed to effective absorption of visible light, abundant exposed catalytic active sites, and suppression of recombination with the assistance of AuNPs. When the same substrate repeats such detection and photocatalytic process twice, the results are similar at per-recyclable detection, indicating that the

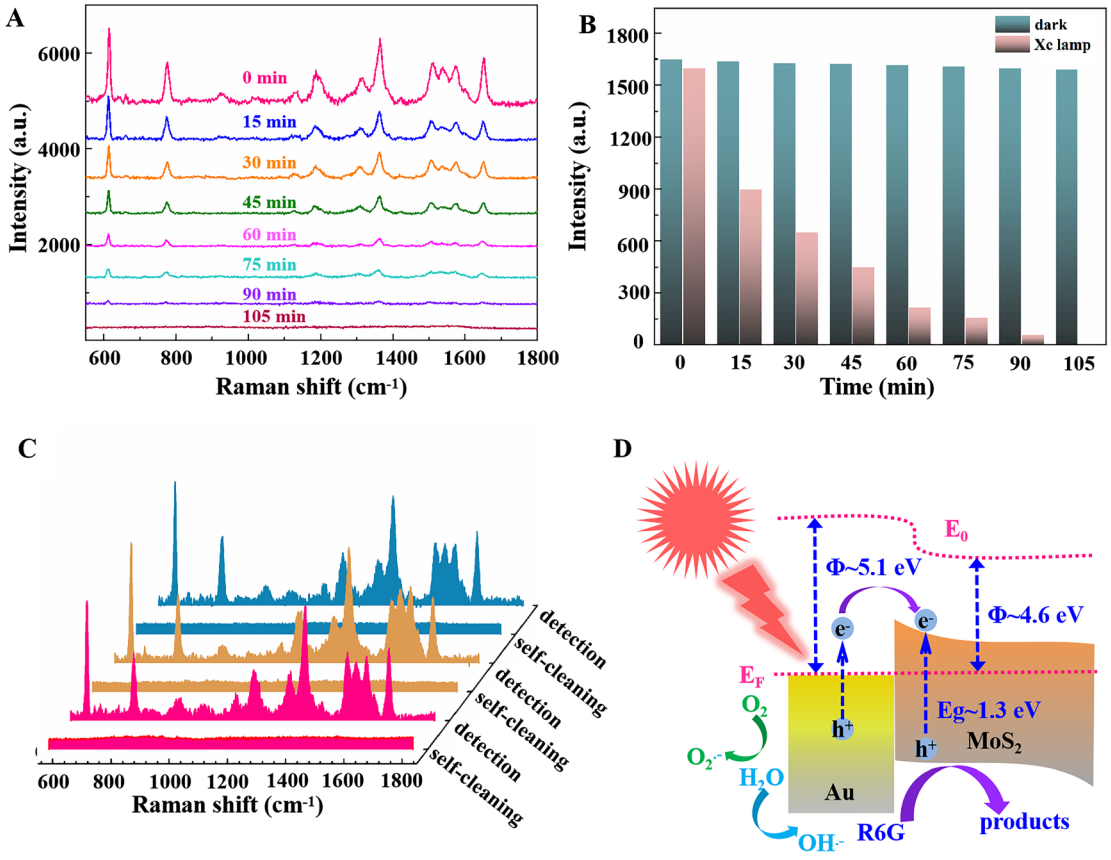

Figure 7: Photodegradation and self-cleaning property.
(A) Surface-enhanced Raman spectroscopy (SERS) spectra of R6G for the pyramid Si (PSi)/ molybdenum disulfide (MoS_2)/Au multiscale cavity (MSC) irradiated by visible light with an interval of 15 min. (B) The intensity of 613 cm^{-1} from the substrate under irradiation and dark with an interval of 15 min. (C) Recycle detection of R6G on the PSi/MoS_2/Au MSC. (D) Illustration of the mechanism of photocatalytic degradation of R6G over PSi/MoS_2/Au MSC.

PSi/MoS_2/Au MSC is feasible as an in situ recyclable SERS substrate.

Based on the aforementioned experiment, the proposed mechanisms of photocatalytic degradation are summarized in Figure 7D. The plasmonic Au and semiconductor MoS_2 act as light absorber under irradiation and the Schottky barrier forms in close contact between them. The hot electrons, induced by plasmon with enough high energies, can overcome the Schottky barrier and transfer from the Au to the MoS_2 conduction band [42]. In addition, the Schottky barrier at the interface of Au and MoS_2 can efficiently prevent the injected hot electrons getting back. During the photocatalytic process, the efficient separation of electron hole pairs has been achieved because of Schottky barrier at the metal/semiconductor interface. Moreover, the vertical-grown MoS_2 nanosheets have plentiful exposed active edge sites for catalytic activity, which offers a large surface area for electron transportation and adsorption. The structure of MSCs can confine the light in the dielectric cavity and improve the utilization of light, further exciting the multiple cavity plasmon modes. The combined effect of MoS_2 nanosheets via strong multiple plasmonic coupling of AuNPs on the active edge sites enhances the visible light photoactivity, which makes recycle utilization come true with a synergistic effect between AuNPs and ultrathin MoS_2 nanosheets.

4 Conclusion

In summary, we have developed a robust PSi/MoS_2/Au MSC hybrid structure leading to the both enhancement of SERS performance and photocatalytic degradation. Through effective coupling of the MoS_2 nanocavity mode on PSi microcavity with the surface plasmons of the AuNPs, the electric field near the cavity walls is greatly enhanced, which was proved by FDTD simulation, and thus a high SERS activity with the EF of ~6.5×10^7 was achieved because of the excellent optical capture capability and abundant electromagnetic “hot spots”.

Meanwhile, the homogeneity and stability were also measured from the hybrid SERS substrate. Through comparing the hydrophobic properties with PSi/MoS_2 MSC and flat-Si/MoS_2/Au, the PSi/MoS_2/Au MSC can realize the directional monitoring of organic pollutant. Furthermore, the PSi/MoS_2/Au MSC, as a visible light self-cleaning SERS substrate, possesses intriguing recycling properties attributed to effective absorption of visible light, plentiful exposed catalytic active sites, and fast charge transfer with the assistance of AuNPs. The proposed strategy for direct growth of hybrid MSCs can pave the way towards SERS- and photodegradation-based applications, holding a great potential in the field of biochemistry for sensing and monitoring.

Author contribution: All the authors have accepted responsibility for the entire content of this submitted manuscript and approved submission.

Research funding: The authors are grateful for financial support from the National Natural Science Foundation of China (11804200, 11974222, 11904214, 11774208), Taishan Scholars Program of Shandong Province (tsqn201812104), Qingchuang Science and Technology Plan of Shandon Qingchuang Science and Technology Plan of Shandong Province (2019KJJ014, 2019KJJ017), a Project of Shandong Province Higher Educational Science and Technology Program (J18KZ011) and China Postdoctoral Science Foundation (2019M662423).

Conflict of interest statement: The authors declare no conflicts of interest regarding this article.

References

[1] Q. Ding, J. Wang, X. Chen, et al., "Quantitative and sensitive SERS platform with analyte enrichment and filtration function," *Nano Lett.*, 2020; vol. 20, pp. 7304–7312, 2020.

[2] W. Yan, L. Yang, J. Chen, Y. Wu, P. Wang, and Z. Li, "In situ two-step photoreduced SERS materials for on-chip single-molecule spectroscopy with high reproducibility," *Adv. Mater.*, vol. 29, p. 1702893, 2017.

[3] S. Asher, "UV resonance Raman spectroscopy for analytical, physical, and biophysical chemistry," *Anal. Chem.*, vol. 65, pp. 59–65, 1993.

[4] Z. Schultz, J. Marr, and H. Wang, "Tip enhanced Raman scattering: plasmonic enhancements for nanoscale chemical analysis," *Nanophotonics*, vol. 3, pp. 91–104, 2014.

[5] J. Yu, Y. Wei, H. Wang, et al., "In situ detection of trace pollutants: a cost-effective SERS substrate of blackberry-like silver/graphene oxide nanoparticle cluster based on quick self-assembly technology," *Opt. Express*, vol. 27, pp. 9879–9894, 2019.

[6] K. Xu, R. Zhou, K. Takei, and M. Hong, "Toward flexible surface-enhanced Raman scattering (SERS) sensors for point-of-care diagnostics," *Adv. Sci.*, p. 1900925, 2019, https://doi.org/10.1002/advs.201900925.

[7] J. Jeong, M. Arnob, K. Baek, S. Lee, W. Shih, and Y. Jung, "3D cross-point plasmonic nanoarchitectures containing dense and regular hot spots for surface-enhanced Raman spectroscopy analysis," *Adv. Mater.*, vol. 28, pp. 8695–8704, 2016.

[8] H. Liu, Z. Yang, L. Meng, et al., "Three-dimensional and time-ordered surface-enhanced Raman scattering hot spot matrix," *J. Am. Chem. Soc.*, vol. 136, pp. 5332–5341, 2014.

[9] X. Zhang, X. Zhang, C. Luo, et al., "Volume-enhanced Raman scattering detection of viruses," *Small*, vol. 15, p. 1805516, 2019.

[10] J. Xu, C. Li, H. Si, et al., "3D SERS substrate based on Au-Ag bimetal nanoparticles/MoS_2 hybrid with pyramid structure," *Opt. Express*, vol. 26, pp. 21546–21557, 2018.

[11] Z. Li, S. Jiang, Y. Huo, et al., "3D silver nanoparticles with multilayer graphene oxide as a spacer for surface enhanced Raman spectroscopy analysis," *Nanoscale*, vol. 10, pp. 5897–5905, 2018.

[12] Z. Dai, X. Xiao, W. Wu, et al., "Plasmon-driven reaction controlled by the number of graphene layers and localized surface plasmon distribution during optical excitation," *Light Sci. Appl.*, vol. 4, p. e342, 2015.

[13] Z. Yang, Q. Li, B. Ren, and Z. Tian, "Tunable SERS from aluminum nanohole arrays in the ultraviolet region," *Chem. Commun.*, vol. 47, pp. 3909–3911, 2011.

[14] S. Tian, Q. Zhou, Z. Gu, X. Gu, and J. Zheng, "Fabrication of a bowl-shaped silver cavity substrate for SERS-based immunoassay," *Analyst*, vol. 138, pp. 2604–2612, 2013.

[15] H. Im, K. Bantz, S. Lee, T. Johnson, C. Haynes, and S. Oh, "Self-assembled plasmonic nanoring cavity arrays for SERS and LSPR biosensing," *Adv. Mater.*, vol. 25, pp. 2678–2685, 2013.

[16] Z. Zuo, S. Zhang, Y. Wang, et al., "Effective plasmon coupling in conical cavity for sensitive surface enhanced Raman scattering with quantitative analysis ability," *Nanoscale*, vol. 11, pp. 17913–17919, 2019.

[17] J. Yu, Y. Guo, H. Wang, et al., "Quasi optical cavity of hierarchical ZnO nanosheets@Ag nanoravines with synergy of near-and far-field effects for in situ Raman detection," *J. Phys. Chem. Lett.*, vol. 10, pp. 3676–3680, 2019.

[18] S. Su, C. Zhang, L. Yuwen, et al., "Creating SERS hot spots on MoS_2 nanosheets with in-situ grown gold nanoparticles," *ACS Appl. Mater. Interfaces*, vol. 6, pp. 18735–18741, 2014.

[19] Z. Zeng, Z. Yin, X. Huang, et al., "Single-layer semiconducting nanosheets: high-yield preparation and device fabrication," *Angew. Chem. Int. Ed.*, vol. 123, pp. 11289–11293, 2011.

[20] E. Er, H. Hou, A. Criado, et al., "High-yield preparation of exfoliated 1T-MoS_2 with SERS activity," *Chem. Mater.*, vol. 31, pp. 5725–5734, 2019.

[21] X. Zhao, J. Yu, Z. Zhang, et al., "Heterogeneous and cross-distributed metal structure hybridized with MoS_2 as high performance flexible SERS substrate," *Opt. Express*, vol. 26, p. 23831, 2018.

[22] F. Xu, B. Zhu, B. Cheng, J. Yu, and J. Xu, "1D/2D TiO_2/MoS_2 hybrid nanostructures for enhanced photocatalytic CO_2 reduction," *Adv. Opt. Mater.*, vol. 6, p. 1800911, 2018.

[23] C. Zhang, S. Jiang, Y. Huo, et al., "SERS detection of R6G based on a novel graphene oxide/silver nanoparticles/silicon pyramid arrays structure," *Opt. Express*, vol. 23, pp. 24811–24821, 2015.

[24] A. Beal and H. Huges, "Kramers-Kronig analysis of the reflectivity spectra of 2H-MoS_2, 2H-$MoSe_2$, and 2H-$MoTe_2$," *J. Phys. C*, vol. 12, p. 881, 1979.

[25] S. Babar and J. Weaver, "Optical constants of Cu, Ag, and Au revisited," *Appl. Opt.*, vol. 54, pp. 477–481, 2015.
[26] C. Schinke, P. Peest, J. Schmidt, et al., "Uncertainty analysis for the coefficient of band-to-band absorption of crystalline silicon," *AIP Adv.*, vol. 5, p. 67168, 2015.
[27] Y. Chen, H. Liu, Y. Tian, et al., "In situ recyclable surface-enhanced Raman scattering-based detection of multicomponent pesticide residues on fruits and vegetables by the flower-like MoS_2@Ag hybrid substrate," *ACS Appl. Mater. Interfaces*, vol. 12, pp. 14386–14399, 2020.
[28] J. Dong, J. Huang, A. Wang, et al., "Vertically-aligned Pt-decorated MoS_2 nanosheets coated on TiO_2 nanotube arrays enable high-efficiency solar-light energy utilization for photocatalysis and self-cleaning SERS devices," *Nano Energy*, vol. 71, p. 104579, 2020.
[29] Y. Shi, J. Wang, C. Wang, et al., "Hot electron of Au nanorods activates the electrocatalysis of hydrogen evolution on MoS_2 Nanosheets," *J. Am. Chem. Soc.*, vol. 137, pp. 7365–7370, 2015.
[30] T. Sreeprasad, P. Nguyen, N. Kim, and V. Berry, "Controlled, defect-guided, metal-nanoparticle incorporation onto MoS_2 via chemical and microwave routes: electrical, thermal, and structural properties," *Nano Lett.*, vol. 13, pp. 4434–4441, 2013.
[31] X. Zheng, Z. Guo, G. Zhang, H. Li, J. Zhang, and Q. Xu, "Building a lateral/vertical 1T-2H MoS_2/Au heterostructure for enhanced photoelectrocatalysis and surface enhanced Raman scattering," *J. Mater. Chem.*, vol. 7, pp. 19922–19928, 2019.
[32] X. Mu and M. Sun, "Interfacial charge transfer exciton enhanced by plasmon in 2D in-plane lateral and van der Waals heterostructures," *Appl. Phys. Lett.*, vol. 117, p. 091601, 2020.
[33] Y. Guo, J. Yu, C. Li, et al., "SERS substrate based on the flexible hybrid of polydimethylsiloxane and silver colloid decorated with silver nanoparticles," *Opt. Express*, vol. 26, pp. 21784–21796, 2018.
[34] C. Zhang, C. Li, J. Yu, et al., "SERS activated platform with three-dimensional hot spots and tunable nanometer gap," *Sens. Actuators B Chem.*, vol. 258, pp. 163–171, 2018.
[35] S. Nie and S. Emory, "Probing single molecules and single nanoparticles by surface-enhanced Raman scattering," *Science*, vol. 275, pp. 1102–1106, 1997.
[36] X. Zhao, C. Li, Z. Li, et al., "In-situ electrospun aligned and maize-like AgNPs/PVA@Ag nanofibers for surface-enhanced Raman scattering on arbitrary surface," *Nanophotonics*, vol. 8, pp. 1719–1729, 2019.
[37] Y. Zhao, X. Pan, L. Zhang, et al., "Dense AuNP/MoS_2 hybrid fabrication on fiber membranes for molecule separation and SERS detection," *RSC Adv.*, vol. 7, p. 36516, 2017.
[38] H. Sun, M. Yao, Y. Song, et al., "Pressure-induced SERS enhancement in a MoS_2/Au/R6G system by a two-step charge transfer process," *Nanoscale*, vol. 11, p. 21493, 2019.
[39] G. Petra, E. Martin, F. B. Simon, V. Jan, T. Nahid, and L. Christoph, "Plasmonic nanofocusing- grey holes for light," *Adv. Phys. X*, vol. 1, pp. 297–330, 2016.
[40] P. Li, D. Pan, L. Yang, et al., "Silver nano-needles: focused optical field induced solution synthesis and application in remote excitation nanofocusing SERS," *Nanoscale*, vol. 11, pp. 2153–2161, 2019.
[41] I. S. Mark, "Nanofocusing of optical energy in tapered plasmonic waveguides," *Phys. Rev. Lett.*, vol. 93, p. 137404, 2004.
[42] B. Shang, X. Cui, L. Jiao, et al., "Lattice-mismatch-induced ultrastable 1T-phase MoS_2-Pd/Au for plasmon-enhanced hydrogen evolution," *Nano Lett.*, vol. 19, p. 2758, 2019.

Supplementary Material: The online version of this article offers supplementary material (https://doi.org/10.1515/nanoph-2020-0454).